Applied Catalysis B: Environmental 170-171 (2015) 43–52

Contents lists available at ScienceDirect

Applied Catalysis B: Environmental

journal homepage: www.elsevier.com/locate/apcatb

Role of MgO over γ-Al_2O_3-supported Pd catalysts for carbon dioxide reforming of methane

Chunkai Shi[a,*], Peng Zhang[b,**]

[a] Department of Chemistry, New Mexico Tech, Socorro, NM 87801, USA
[b] Department of Chemistry, University of Cincinnati, Cincinnati, OH 45221, USA

ARTICLE INFO

Article history:
Received 20 November 2014
Received in revised form 17 January 2015
Accepted 24 January 2015
Available online 28 January 2015

Keywords:
Carbon dioxide reforming of methane
Pd catalyst
MgO additive
Decoration effect

ABSTRACT

A series of Pd/Al_2O_3 catalysts with varying Mg loading (1, 3, 7 and 10 wt%) were investigated for carbon dioxide reforming of methane. It was observed that the initial catalytic activities and long-term stabilities in terms of both CO_2 and CH_4 conversions increased with increasing Mg content when its loading was below 7 wt%. When Mg content was up to 10 wt%, the initial activity and stability decreased. Moreover, Pd7Mg/Al_2O_3 displayed the highest H_2 and CO yields. Characterization results conducted on catalysts before and after reaction test demonstrated that MgO mainly presented in amorphous form for catalysts with additive content below 7 wt%; while a fraction of MgO transformed into crystalline form when more additive was introduced to the catalyst. The amorphous MgO significantly enhanced surface metal dispersion, decreased average Pd crystallite size and thus improved resistances against both metal sintering and carbon deposition, which contributed to the enhanced initial activities and long-term stabilities. On the contrary, the crystalline MgO decreased exposed Pd active sites, caused metal sintering and thus led to increased amount of carbon deposition owing to both its negative decoration effect on surface metal and deterioration effect on textural characteristics of support. These factors were responsible for the worse catalytic performance of Pd10Mg/Al_2O_3 as compared to that of Pd7Mg/Al_2O_3.

1. Introduction

CO_2 is the most important anthropogenic greenhouse gas, and its emission in large quantities from the flue gas of industrial combustion of fossil fuel (coal, oil and natural gas) predominantly leads to global warming affecting the quality of our living environment and becoming worldwide concern [1]. In U.S., CO_2 is ~84% of all greenhouse gas emissions, and coal fired power plants releases the largest quantity in their flue gas, accounting for one third of total man-made CO_2 [2]. Therefore, while it is important to reduce the greenhouse gas emission, it is also important to find ways to remove the greenhouse gas. One of the promising technologies is to chemically convert CO_2 in the flue gas to other carbon species that lead to highly valuable chemical products. A hopeful reaction along this line of thought is the reaction between CO_2 and CH_4 ($CH_4 + CO_2 \rightarrow 2CO + 2H_2$, $\Delta H^\circ_{298} = +247\ kJ\ mol^{-1}$) referred to as dry reforming of methane. There are potentially several advantages in integrating this reaction into coal-fired power plants. First, it converts CO_2 into synthesis gas (syngas), which can either be directly used as fuel for combustion turbine of the power plant or as the starting materials in the well-known Fischer–Tropsch (FT) synthesis [3,4], producing various value-added liquid hydrocarbons and oxygenates. Second, the above forward reaction is endothermic, which can potentially take advantage of the high temperature of the flue gas (500–700 °C) [5]. Last, but not least, it simultaneously helps reduce methane, another important greenhouse gas. The methane reforming process, if successfully developed, should be well suited for carbon capture and sequestration and have great implication in reducing greenhouse gas emissions.

A main drawback with carbon dioxide reforming of methane at 500–700 °C is the conversion of product hydrogen to water through reverse water–gas shift reaction (RWGS), which is thermodynamically favorable and rapid to reach equilibrium in the temperature range [6,7]. The problem persists due to the lack of an effective catalyst. Moreover, current studies on carbon dioxide reforming of methane mainly focused on the development of Ni and Co catalysts due to their availabilities and low costs [8–13]. Unfortunately, these existing catalysts require high metal loading or high reaction

* Corresponding author. Tel.: +1 5135569222.
** Corresponding author. Fax: +1 513 556 9239.
E-mail addresses: chunkaishi@yahoo.com, cshi@nmt.edu (C. Shi), peng.zhang@uc.edu (P. Zhang).

http://dx.doi.org/10.1016/j.apcatb.2015.01.034
0926-3373/

temperatures (usually ≧800 °C) to achieve high activity, selectivity and stability. At operation temperatures of <700 °C, they tend to show poor catalytic performance due to metal sintering and severe carbon deposition. It is necessary, therefore, that other kinds of catalyst with excellent performance be investigated for the integration of the reforming process.

Recently, Pd catalyst employed to carbon dioxide reforming of methane has attracted increasing attention thanks to its strong ability to activate CH_4 and high catalytic performance [3,14]. Among Group VIII metals, Pd shows the strongest ability to activate the C—H bond of CH_4 [14], and the C—H bond activation is suggested as the elemental reaction step in the reforming process [3]. Supported Pd catalysts, such as Pd/SiO_2, Pd/Al_2O_3 and Pd/TiO_2, have shown high conversion activities of CH_4 and CO_2 at relatively low temperatures (250–700 °C) [15–18]. On the other hand, deactivation of Pd catalysts is still a problem, caused by coking deposition on their active metal surfaces and by structural transformations, sintering and recombination of the active components under reaction conditions. Carbon deposits usually develop on the surfaces of metal particles through two reactions: (i) methane decomposition to carbon and hydrogen ($CH_4 \rightarrow C + 2H_2$), and (ii) disproportionation of carbon monoxide to carbon and carbon dioxide ($2CO \rightarrow C + CO_2$) [3,4]. Many publications have reported that non-promoted Pd catalysts suffer significant deactivation due to metal sintering and severe carbon deposition [18–20]. Considerable efforts are dedicated to overcoming these drawbacks. One of the effective ways is to introduce a second metal to the catalysts. Addition of Ce to $Pd/\alpha Al_2O_3$ distinctly increased activity and stability of catalyst at 627 °C due to suppressing carbon deposition and decreasing Pd sintering [18]. Alkaline earth and rare earth metals (Ba and La) were also found to improve the catalytic stability of Pd/Al_2O_3 in carbon dioxide reforming of methane at 750 °C [21], which was ascribed to the decrease of the deposited coke amount. Introducing Ni to Pd/MCM-41 catalysts improves metal–support interaction and leads to small particle size and high metal dispersion, accounting for enhanced catalytic performance [22]. Promoter amount plays a key role in controlling the surface properties of the noble metal catalysts, which determine the catalytic performance in methane reforming reactions.

Support also plays an important role for Pd catalyst employed to the reforming reaction [14,19]. γ-Al_2O_3 is one of the most widely used supports because of its high surface area, good mechanical property and low cost. Its high surface area and surface structure could ideally offer high metallic Pd dispersion [23]. However, strong Lewis acidity of γ-Al_2O_3 potentially makes supported Pd particles prone to sintering under high temperature condition, causing carbon deposition and activity loss of catalyst. Therefore, introduction of a basic component to γ-Al_2O_3 is suggested to compensate the negative effect of its acidity on metal Pd and to simultaneously improve activation of the reactant, CO_2. MgO is one of the most widely studied promoter for Ni catalysts with acidic supports, such as γ-Al_2O_3 [24,25], SiO_2 [26], and HY [27], in carbon dioxide reforming of methane as it could improve metal Ni dispersion, support structure, metal–support interaction, carbon deposition resistance and even activation of CO_2. In addition, significant beneficial effect of Mg promoter on Pd/Al_2O_3 catalysts are widely reported for other important reactions such as methane combustion [28], enhanced selectivity in partial hydrogenation of acetylene due to improved Pd dispersion [29], and direct oxidative esterification of aldehydes with alcohols to esters [30].

This report is a continuation of our previous study on Pd catalysts with various kinds of additives used for carbon dioxide reforming of methane. Here we focus on the effect of varying Mg loading on both surface characteristics of nanostructured γ-Al_2O_3-supported Pd catalyst and its catalytic performance. It would be shown that introducing an optimal Mg amount to Pd/Al_2O_3 could enhance surface Pd dispersion, decrease metallic particle size, and therefore, greatly improve its catalytic performance via increasing surface active sites and strengthening resistances to both carbon deposition and metal sintering.

2. Experimental

2.1. Catalyst preparation

γ-Al_2O_3-supported Pd catalysts with and without Mg modification were prepared by incipient wetness impregnation method in one step using calculated amounts of palladium nitrate and magnesium nitrate (both from Alfa Aesar) solutions. Before impregnation, γ-Al_2O_3 pellet (from Alfa Aesar) was crushed and sieved to 20–40 mesh sizes and then calcined at 500 °C for 3 h. The γ-Al_2O_3 powder was thoroughly mixed with the solutions and kept at room temperature for 12 h, followed by drying at 120 °C for another 12 h and calcining at 700 °C for 2 h in static air. The loadings of metal Pd and Mg were 1 wt%, and 1–10 wt%, respectively. Catalysts are designated as PdxMg/γ-Al_2O_3 where *x* stands for Mg loading in weight percentage.

2.2. Catalyst characterization

The BET specific surface area, pore size and distribution of samples, which were reduced previously in hydrogen at 700 °C for 2 h, were tested at liquid nitrogen temperature using a Micromeritics ASAP-2020 instrument. All samples were degassed at 400 °C for 4 h prior to the measurement to remove the adsorbed moisture.

X-ray powder diffraction patterns of both freshly reduced at 700 °C and spent samples were recorded on a Siemens D500 diffractometer using Ni-filtered Cu Kα radiation with λ = 1.5418 Å in θ–2θ scan mode, run at 40 kV and 30 mA. Step size and step scan time were 0.02° and 3 s, respectively.

CO chemisorption of catalyst samples was measured using the Micromeritics ASAP-2020 instrument for determining Pd dispersion and surface metal area, again after they had been reduced in hydrogen at 700 °C for 2 h. The sample was first degassed at 400 °C for 4 h and then cooled down, weighted and moved to a U-shape measurement tube. Prior to CO chemisorption, the sample was evacuated at 100 °C for 1 h, followed by in situ reducing in hydrogen at 400 °C for 2 h and then evacuating at 100 °C for another hour. Finally, isotherm of CO chemisorption was conducted at 35 °C. The Pd dispersion and surface metal area were calculated based on the stoichiometry of Pd/CO = 1.

Thermal stability of PdO species was studied by a temperature-programmed desorption of oxygen (O_2-TPD) method under UHP He (99.999%) atmosphere. Sample of around 100 mg was loaded into a quartz tube reactor with a *K*-type thermocouple contacting the bottom of the sample. Prior to the desorption test, the sample was purged with UHP He flow of 30 ml/min for 1 h at room temperature. The O_2-TPD run was then carried out by heating the sample in the same He flow at a ramp rate of 10 °C/min. Desorbed gases were monitored with a QSM200 mass spectrometer (SRS, Inc.).

Carbon species deposited on spent catalysts was investigated by temperature-programmed oxidation (TPO) method. Around 50 mg of sample was loaded into the quartz reactor. After purged in a dry air flow (30 ml/min) for 30 min, sample was heated in same air flow at a ramp rate of 10 °C/min. The reaction product, CO_2 (m/e = 44), was monitored using the QMS200 gas analyzer. The amount of carbon deposition was estimated from the obtained CO_2 peak area, which was quantified by using peak area of known volumes of CO_2.

Raman spectra of spent catalysts were obtained using a LabRAM Raman microscope (HORIBA Jobin Yvon Inc.) with the following operation parameters: a He–Ne laser source of 632.8 nm as exci-

tation source, laser intensity of ~2 mW, 10 s acquisition time, and a total of 10 accumulation per spectrum. Before sample measurement, Raman spectrum was calibrated using a silicon wafer peak at 520.7 cm^{-1}. All samples were analyzed under an atmospheric condition without pre-treatment.

Transmission electron microscope (TEM) images and energy-dispersive X-ray (EDX) spectra of spent catalyst were obtained on a JEOL 2010 instrument operated at an accelerating voltage of 200 kV. The sample was prepared by dropping and drying the spent catalyst, which was dispersed in anhydrous ethanol by sonication, on holey carbon-coated Cu grids.

2.3. Catalyst evaluation

The carbon dioxide reforming of methane was carried out in a fixed-bed continuous flow quartz reactor at atmospheric pressure and a gas hourly space velocity (GHSV) of 24,000 ml g^{-1} h^{-1}. All gas flow rates were controlled by GFC mass flow controllers (Aalborg Inc.). Typically, 100 mg of sample was loaded into the reactor of 4 mm ID. Sample temperature was monitored using a *K* type thermocouple in contact with the bottom of sample layer. Before the reaction, the sample was in situ reduced by UHP H_2 with a flow rate of 13 ml/min at 700 °C for 2 h and then cooled down to room temperature in H_2. After purged by He (20 ml/min) for 30 min, the mixed feedstock gases (CH_4:CO_2:He = 1:1:2 ml/min) were introduced to the catalyst bed. The reaction temperature was raised from room temperature to 700 °C at a ramp rate of 10 °C/min. Subsequently, the reaction temperature was held at 700 °C for stability test. Reactant and product gases were analyzed simultaneously by on-line both QMS200 gas analyzer with capillary sampling and gas chromatograph (Buck 910) equipped with a CARBOXEN 1000 column and a thermal conductivity detector. The detected mass-to-charge ratios (*m*/*e*) are 44, 2, 28 and 15 for CO_2, H_2, CO and CH_4, respectively. A data collection model of pressure via time (*P* vs *T*) was used for a continuous on-line monitoring of various gas constituents.

3. Results and discussion

3.1. Catalyst characterization before reaction

3.1.1. Textural properties

The N_2 adsorption–desorption isotherms of reduced catalysts and pure γ-Al_2O_3 support are shown in Fig. 1. Their specific textural characteristics are summarized in Table 1. According to IUPAC classification [31], all samples show an IV type isotherm with a H2-shaped hysteresis loop, typical for mesoporous materials. Note that the supported-Pd catalysts without or with 1 wt% Mg loading did not show a noticeable change in the textural characteristics as compared to those of the Al_2O_3 support. This indicates that low Mg loading has a good stability effect on the textural properties of Al_2O_3 support. However, with increase of Mg loading from 3 to 10 wt%, the surface area, pore volume and pore size of the catalysts showed gradual decrease. Pd10Mg/Al_2O_3, specifically, showed significant decrease and had the lowest values of surface area, pore volume and pore size, with values decreasing around 16.0, 26.6 and 12.4%, respectively, from those of Al_2O_3 support. The decrease is probably attributed to surface covering and some pore blocking of support caused by addition of Mg additive, similar to what have been reported of different additive content on the textural properties of support [22,32].

Table 1
Textural properties of support and catalysts.

Sample	Surface area (m^2/g)	Pore volume (cm^3/g)	Pore size (nm)
γ-Al_2O_3	199.4	0.61	12.9
Pd/Al_2O_3	199	0.6	12.7
Pd1Mg/Al_2O_3	198.8	0.59	12.6
Pd3Mg/Al_2O_3	190.4	0.55	12.1
Pd7Mg/Al_2O_3	179.5	0.51	11.7
Pd10Mg/Al_2O_3	168.1	0.45	11.3

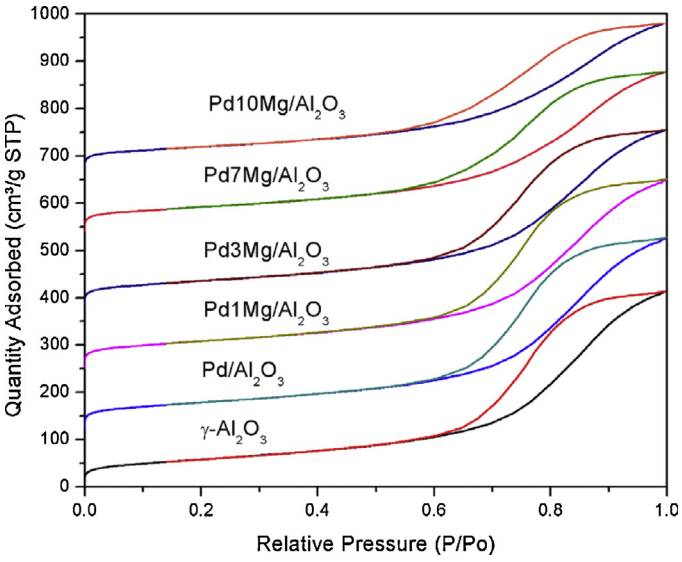

Fig. 1. N_2 adsorption–desorption isotherms of reduced catalysts.

3.1.2. XRD

XRD patterns of catalysts are shown in Fig. 2. As expected, a strong diffraction peak (2θ = 40.1°) assigned to the metal Pd (1 1 1) plane was observed for all samples (JCPDS 05-0681). Based on the Scherrer equation, average Pd crystallite size of catalyst was estimated and the results are listed in Table 2. It is interesting to note that all Mg-modified Pd catalysts showed a smaller metal particle size, and the particle size decreased with increasing Mg content, reaching the minimum value (~10 nm) at 7–10 wt% Mg content as compared to that of Pd/Al_2O_3 (17.9 nm).

All samples displayed characteristic diffraction peaks (2θ = 66.7°, 45.8° and 37.6°) of γ-Al_2O_3 (JCPDS 10-0425), which gradually shift to lower 2θ values as Mg content increases. This

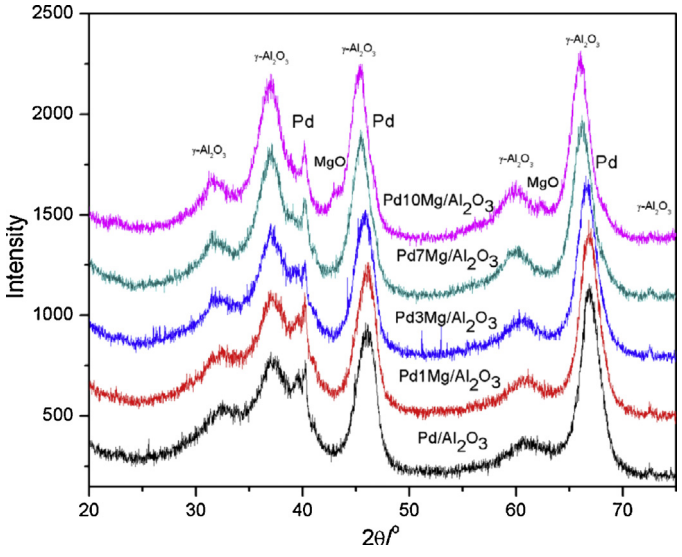

Fig. 2. XRD profiles of catalysts reduced before reaction.

could be attributed to enrichment of MgO species on the surface of catalysts resulting in the structure distortion of γ-Al_2O_3. A similar trend for the diffraction angle shift to a lower value has been previously observed for PdNi/MCM-41 catalyst [22]. The signals that would have been assigned to Mg-containing species, such as MgO and $MgAl_2O_4$ spinel etc., were not detected for samples with 1, 3 or 7% Mg addition, suggesting that the surface Mg species on these catalysts be either amorphous structure or highly dispersed. However, in the case of Pd10Mg/Al_2O_3, two diffraction peaks corresponding to MgO at $2\theta = 43.0$ and 62.3° (JCPDS 04-0829) were detected, indicating that a portion of MgO transformed to crystalline structure under the present reduction condition. Meanwhile, it is worthwhile to point out that there is no observable evidence in the XRD to indicate the formation of Pd–Mg alloy compound for all Mg-containing catalysts. Pd has a lower surface tension, a larger atomic radius and much less loading than Mg. As a result, there is a trend that Pd is expelled out of the MgO matrix. This agrees with the previous reports where similar Pd-containing alloy compounds are excluded in supported Pd–Ni, Pd–Cu and Pd–Zn catalysts [19,33,34].

3.1.3. CO-chemisorptions

CO chemisorption is an important method to characterize metal dispersion and surface area of active components, which are closely related to performance of supported metal catalysts. Table 2 lists the values of Pd dispersion and metal area of the reduced catalysts, which were determined by the amounts of irreversibly adsorbed CO. We also carried out a comparative test over 7 wt% Mg-loaded γ-Al_2O_3 without Pd; no observable amount of CO was consumed. Thus, the CO amount consumed over catalysts was adsorbed solely on surface Pd component. As seen in Table 2, the Pd dispersion and metal area increased considerably with 1 wt% Mg loading and continuously with more Mg loading, then reached a maximum at 7 wt% Mg loading, and finally decreased with more Mg loading up to 10 wt%. The maximum Pd dispersion and metal area for Pd7Mg/Al_2O_3 were ~2.5 folds those of Pd/Al_2O_3. Generally, sintering is a main reason to cause agglomeration of surface metal component and results in decrease of surface dispersion and metal area. Depending on different adding contents, Mg additive can improve the sintering resistance of catalyst to some extent under the reduction condition. It is interesting that Pd7Mg/Al_2O_3 and Pd10Mg/Al_2O_3 displayed a significant difference in the Pd dispersion and metallic surface area values, but their average metallic crystallite sizes from Table 2 were close. This disagreement could be explained by the decoration effect where crystalline MgO on Pd10Mg/Al_2O_3, which was confirmed by XRD results and has a larger particle diameter than the amorphous one, would migrate and subsequently cover part of Pd crystallites. Similar effect has been reported for CeO_2-modified Pd/Al_2O_3 and La_2O_3-promoted Pt/Al_2O_3, where partially reduced CeO_x or LaO_x covered a portion of Pd or Pt particles leading to decrease of metallic surface dispersion [35,36].

Table 2
The Pd dispersion, metallic surface area and particle size of catalysts.

Catalysts	Pd dispersion (%)	Metallic surface area (m^2/g metal)	Pd particle size (nm)	
			$D1_{XRD}$[a]	$D2_{XRD}$[a]
Pd/Al_2O_3	9.3	41.4	17.9	27.9
Pd1Mg/Al_2O_3	19.6	87.3	16.2	18.5
Pd3Mg/Al_2O_3	20.7	92.2	12.9	15.9
Pd7Mg/Al_2O_3	23	102.5	10.1	11.7
Pd10Mg/Al_2O_3	13.9	62.2	10.7	16.7

[a] *D*1 and *D*2 stand for the Pd particle sizes of catalysts determined by XRD before and after reaction, respectively.

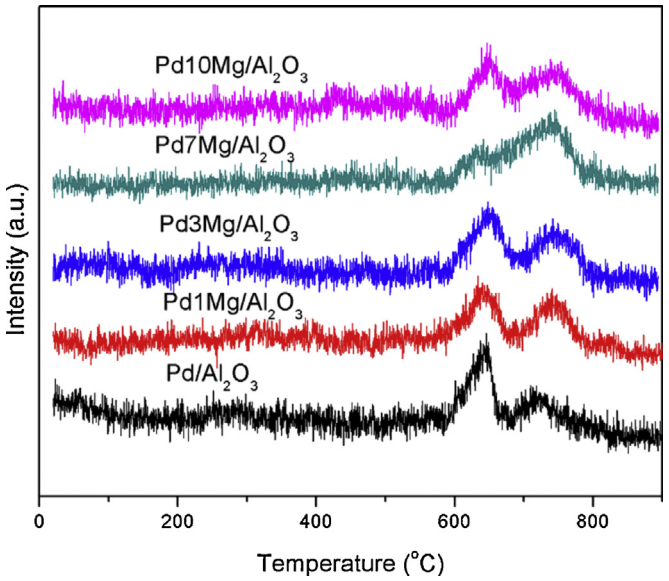

Fig. 3. O_2-TPD profiles of catalysts (test conditions: He flow rate = 30 ml/min; heating rate = 10 °C/min).

3.1.4. O_2-TPD

Additive Mg modified surface properties of the supported Pd, such as crystallite size and surface dispersion. The surface property depends on the interaction between Pd species and support. It is well known that the stronger the Pd—O bond in PdO, the stronger interaction between PdO and support. Therefore, the effect of Mg loading on thermal stability of supported PdO species is investigated by temperature programmed desorption of oxygen (O_2-TPD). As shown in Fig. 3, all samples clearly exhibited twin desorption peaks between ca. 600 and 800 °C, which could be ascribed to oxygen evolution from decomposition of PdO species into metallic palladium since Pd—O bond becomes thermodynamically unstable around the temperature range under O_2-free atmosphere [28,37–39]. According to the literatures [40–42], the oxygen evolution peak at the lower temperature was due to decomposition of bulk PdO species under weak interaction with support, while the one at the higher temperature was associated with decomposition of highly dispersed PdO species under strong interaction with support. For Pd/Al_2O_3, a large desorption peak was observed at ca. 640 °C and a small one at 715 °C. It is clearly seen that the relative ratio of the low and high temperature desorption peaks depends on the additive loading. With addition of Mg to Pd/Al_2O_3, the relative ratio of the high temperature desorption peaks significantly increased, and their temperature at peak top also shifted to higher values (ca. 745 °C). Notably, of all samples Pd7Mg/Al_2O_3 showed the largest desorption peak at high temperature and the smallest desorption peak at low temperature, implying a kind of interaction occurred between Pd species and support.

3.2. Initial activity of catalysts

Initial activities of the catalysts in CO_2 reforming of CH_4 to syngas were studied in the mixed feedstock gases of $CO_2/CH_4/He = 1/1/2$ under atmospheric pressure and a weight hourly space velocity of 24,000 ml g^{-1} h^{-1}. A comparative test over Mg-modified Al_2O_3 (7 wt% Mg loading on Al_2O_3) was also carried out under the same conditions, showing no observable conversion of methane and carbon dioxide. Initial conversions of CH_4 and CO_2, yields of H_2 and CO as well as selectivity ratio of H_2 and CO at different reaction temperatures for all catalysts, are listed in Table 3. The addition of Mg to Pd/Al_2O_3 significantly enhanced the initial CH_4

Table 3
Effect of reaction temperature on catalytic performance of catalysts for CO_2 of CH_4 (reaction conditions: GHSV = 24,000 mlg^{-1} h^{-1}; $CH_4/CO_2/He = 1:1:2$; $P = 1$ atm).

Catalyst	$T_{react.}$(°C)	CO_2(%)	CH_4(%)	H_2 yield (%)	CO yield (%)	H_2/CO (selectivity ratio)
Pd/Al_2O_3	500	24.7	20.5	10.8	16.6	0.72
	550	43.8	37.6	22	31.1	0.77
	600	62.8	57	36.3	45.6	0.83
	650	77.2	74.4	50.1	59	0.86
	700	85.5	84.2	60.1	66.8	0.9
$Pd1Mg/Al_2O_3$	500	27.4	22.5	12.2	18.1	0.75
	550	47.1	40	24	32.5	0.81
	600	66.8	60.4	39.1	48.4	0.85
	650	81.4	78.3	53.6	61.2	0.89
	700	88.8	87.6	59.6	67.4	0.92
$Pd3Mg/Al_2O_3$	500	29.7	24.1	12.6	20.1	0.7
	550	48.8	42.5	24.5	35.5	0.74
	600	68.1	62.6	38.8	51.6	0.78
	650	82.2	79.6	51.5	64.4	0.81
	700	89.2	88.6	59.3	69.6	0.84
$Pd7Mg/Al_2O_3$	500	33.8	26.9	14.9	23.3	0.72
	550	53.9	46	28.2	39.2	0.78
	600	71.2	65.4	42.6	54.2	0.82
	650	83.4	80.9	54.4	64.9	0.85
	700	89.4	89	61.7	70.2	0.88
$Pd10Mg/Al_2O_3$	500	26	21.1	11	17.2	0.72
	550	44.6	38.4	21.9	30.7	0.77
	600	64.4	57.9	36.2	45.8	0.83
	650	80	75.3	50.1	53.1	0.89
	700	88.6	86.5	60.1	67.4	0.91

and CO_2 conversions at different temperatures, with increase in the order: $Pd/Al_2O_3 < Pd10Mg/Al_2O_3 < Pd1Mg/Al_2O_3 < Pd3Mg/Al_2O_3 < Pd7Mg/Al_2O_3$. There appears to be an optimal Mg loading, beyond which further Mg loading increase would lead to decrease in the catalytic activity. $Pd7Mg/Al_2O_3$ showed the highest CH_4 and CO_2 conversions as well as the highest yields of H_2 and CO at different temperature. Although the initial activities of Mg-modified catalysts had a small difference, $Pd7Mg/Al_2O_3$ and Pd/Al_2O_3 still displayed a significant activity difference (10.1% in CO_2 conversion at 550 °C and 8.4% at 600 °C). The activity difference was higher than those previously reported in the literatures [43,44]. For example, the largest difference of CO_2 conversion at 600 °C between catalysts is <5% in the Ref. [43]. On the other hand, in agreement with previous publications [9,20], even if the reaction proceeds at the stoichiometric ratio (1:1) of reactants, the CO_2 conversion was obviously higher as compared to the CH_4 conversion, especially at relatively low temperature (<650 °C). When reaction temperature reached 700 °C, the CH_4 and CO_2 conversions of catalyst became closer than those at temperatures below 650 °C. The H_2/CO values for all catalysts were found to increase with increasing reaction temperature and to gradually approach one. These observations could be mainly attributed to concomitance of RWGS along with the reforming process. The RWGS reaction is thermodynamically favorable between 500 and 700 °C, and is gradually limited with increasing reaction temperature [6,7].

It is noticed that Mg modification causes the decrease of specific surface area and pore size of Pd/Al_2O_3 catalyst (Table 1). Yet the decrease apparently does not reduce the initial activity of catalysts because all Mg added catalysts show better catalytic performance than Pd/Al_2O_3. Therefore, the initial activity of catalysts appears to be solely linked to characteristics of surface Pd species, such as metal dispersion, specific metal area and particle size (Table 2), rather than the specific surface area and pore size of catalysts. This point is further illustrated by the good linear correlation between the metallic Pd surface area and the catalysts' activities at 600 °C (Fig. 4). $Pd7Mg/Al_2O_3$ with the highest metallic surface area (S_{Pd} = 102.5 m^2/g) showed the highest CO_2 conversion. In contrast, Pd/Al_2O_3 shows the lowest CO_2 conversion due to its lowest metallic surface area (S_{Pd} = 41.4 m^2/g). These results suggest that active sites for the reforming reaction are located on reduced Pd and initial activity is closely associated with the amount of exposed metallic surface area. Higher Pd dispersion and metallic surface area would create more active sites, leading to higher initial activity for the catalytic reaction.

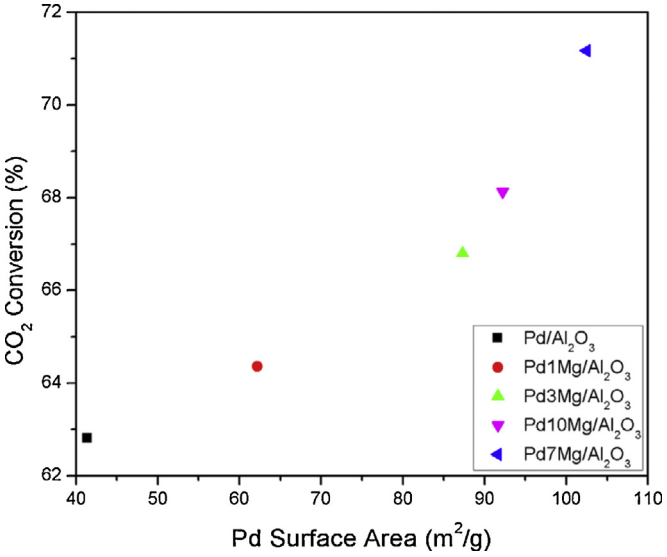

Fig. 4. CO_2 conversion of catalyst as a function of metallic surface area (reaction temperature = 600 °C).

3.3. Reaction stability of catalysts

The long-term reaction stability of catalyst was investigated at 700 °C. As presented in Figs. 5 and 6, significant differences for the CH_4 and CO_2 conversions of catalysts can be clearly observed with increasing time on stream. Pd/Al_2O_3 had a decent initial conversion activity, but it dramatically deactivated and the

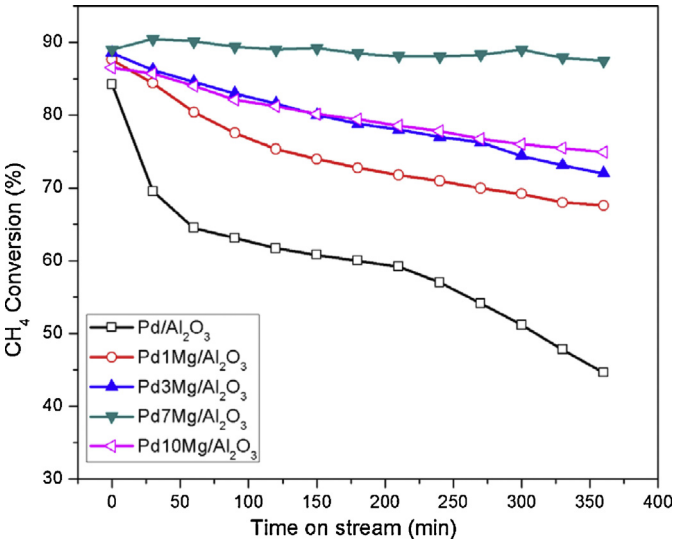

Fig. 5. Effect of reaction time on the CH_4 conversion of catalysts in CO_2 reforming of CH_4 (Reaction conditions: GHSV = 24,000 ml g^{-1} h^{-1}, $CH_4/CO_2/He$ = 1:1:2, P = 1 atm, T = 700 °C).

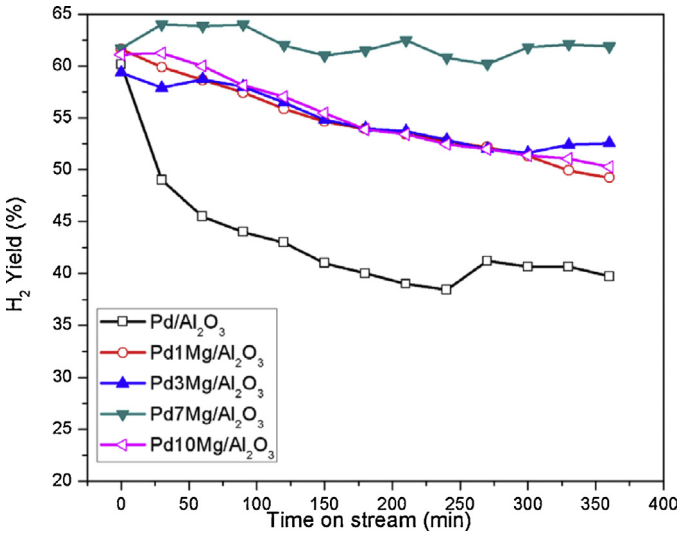

Fig. 7. H_2 yields of catalysts during stability test in CO_2 reforming of CH_4.

reaction almost stopped after a short period of time. Thus, the current stability tests over all catalysts only lasted for 6 h, similar to those in the reported literatures where stability evaluation of catalyst with ≦6 h is conducted [12,44–46]. The conversion values of CH_4 and CO_2 over Pd/Al_2O_3 quickly dropped to 44.6 and 36.2% at the end of test from 84.2 and 85.5% at the beginning of test, respectively, exhibiting the lowest conversion efficiency and the fastest deactivation trend. On the contrary, Mg-modified catalysts regardless of loaded Mg amount showed much better stabilities of reactant conversions than the unmodified one. Noticeably, no significant activity loss was found for $Pd7Mg/Al_2O_3$ during the time on stream. It was capable of reaching CH_4 conversion between 87.5 and 90.5% as well as CO_2 conversion between 88.5 and 90.5%, showing the highest conversion efficiency and the best catalytic stability. Overall, the activity stability followed in the order: $Pd/Al_2O_3 < Pd1Mg/Al_2O_3 < Pd3Mg/Al_2O_3 < Pd10Mg/Al_2O_3 < Pd7Mg/Al_2O_3$. Moreover, comparing the activity data of each catalyst, it was found that the CH_4 conversion was higher than the CO_2 conversion after ~1 h of time on stream for Pd/Al_2O_3 and $Pd3Mg/Al_2O_3$, whereas the two conversions over other catalysts remained close until the end of the test. The observation may be ascribed to the occurrence of significant methane cracking ($CH_4 \rightarrow C + 2H_2$) over Pd/Al_2O_3 and $Pd3Mg/Al_2O_3$ as the reforming reaction proceeds.

The selectivity ratio of H_2/CO and the yields of H_2 and CO as a function of time on stream are shown in Figs. 7–9. The highest and most stable product yields and the most stable H_2/CO ratio were obtained for $Pd7Mg/Al_2O_3$. The results are in line with its highest activity stability owing to both strong carbon and Pd sintering resistances. Conversely, other catalysts showed much more decrease in product yields and more oscillation in the H_2/CO ratio. This could be due to their unstable and declined conversions of CH_4 and CO_2 caused by carbon deposition and Pd sintering. On the other hand, the average H_2/CO ratio for all catalysts deviated from the stoichiometric value of unity of the dry reforming. This indicates concomitance of some side reactions along with the reforming reaction. Previous publications suggested that in addition to RWGS ($CO_2 + H_2 \rightarrow CO + H_2O$, $\triangle H^{\circ}_{298k}$ = 41 kJ/mol) flowing side reactions might occur under the present reforming conditions, which affects

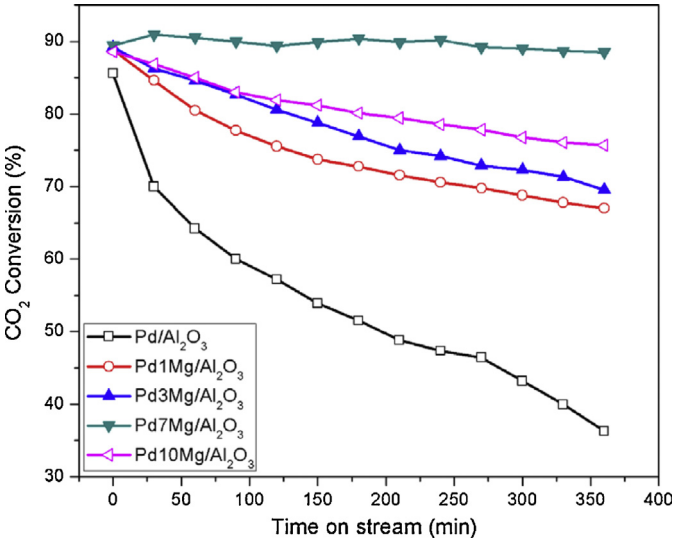

Fig. 6. Effect of reaction time on the CO_2 conversion of catalysts in CO_2 reforming of CH_4 (Reaction conditions: GHSV = 24,000 ml g^{-1} h^{-1}, $CH_4/CO_2/He$ = 1:1:2, P = 1 atm, T = 700 °C).

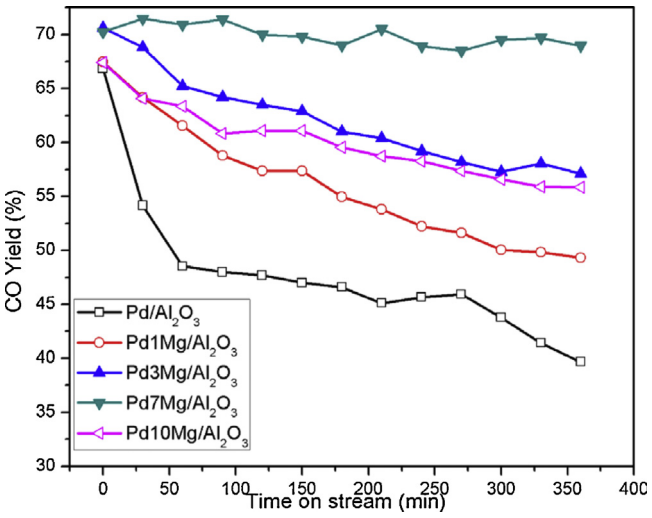

Fig. 8. CO yields of catalysts during stability test in CO_2 reforming of CH_4.

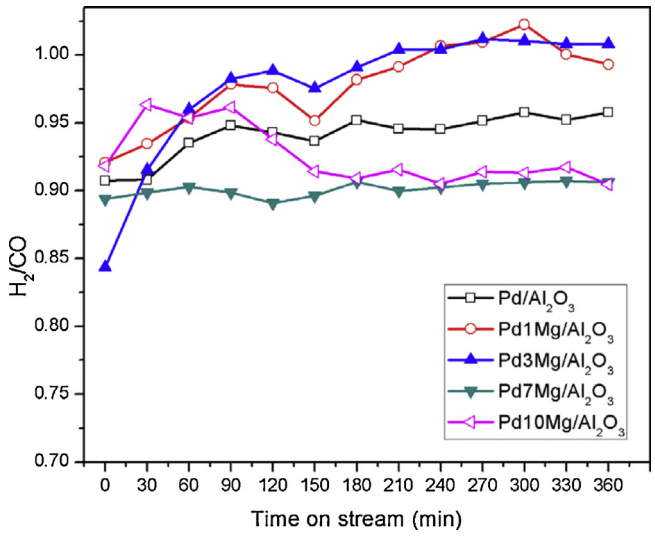

Fig. 9. H_2/CO ratio as a function of reaction time over Pd catalysts.

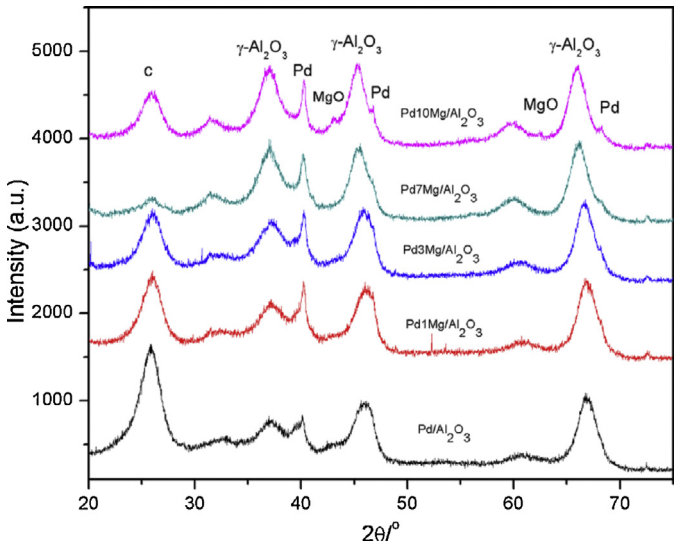

Fig. 10. XRD patterns of spent catalysts.

the selectivity and contribution of reaction products, H_2 and CO [47,48].

$$CH_4 \rightarrow C + 2H_2,\ \Delta H^{\circ}_{298k} = 75\ \text{kJ/mol}$$

$$CO \rightarrow C + CO_2,\ \Delta H^{\circ}_{298k} = -171\ \text{kJ/mol}$$

$$CO + H_2 \rightarrow C + H_2O,\ \Delta H^{\circ}_{298k} = -131\ \text{kJ/mol}$$

For the present reaction system, these side reactions could take place to different extent. In the cases of $Pd7Mg/Al_2O_3$ and $Pd10Mg/Al_2O_3$, RWGS could be the main side reaction but not severe as their CO_2 conversions equaled to or were slightly higher than CH_4 conversions, and their H_2/CO ratio was close to 1 (≥0.9) during the stability test. For Pd/Al_2O_3, $Pd1Mg/Al_2O_3$ and $Pd3Mg/Al_2O_3$, the occurrence of the methane cracking could be more significant than RWGS and CO disproportionation (Boudouard reaction) since their CO_2 conversions equal to or are slightly lower than CH_4 conversions, and their average H_2/CO ratio was larger than that of $Pd7Mg/Al_2O_3$ or $Pd10Mg/Al_2O_3$. Moreover, oscillation of the H_2/CO ratio value implies the occurrences of these side reactions to different extent.

3.4. Characterization of catalysts and carbon deposition after reaction

XRD patterns of spent catalysts are depicted in Fig. 10. Average Pd crystallite sizes of the spent catalysts were estimated according to Scherrer equation and listed in Table 2. Upon compared to freshly reduced catalyst, spent catalyst showed larger Pd crystalline size, suggesting occurrence of metal sintering during the long-term stability test. Pd/Al_2O_3 showed the largest increase in Pd particle size after reaction, implying that addition of Mg to the catalyst effectively suppresses the sintering of active metal. The suppressing effect depends on the Mg loading of catalyst. $Pd7Mg/Al_2O_3$ displayed the smallest increase (about 1.6 nm) of average Pd crystallite size, illustrating its best sintering-resistant ability. In addition, all spent catalysts had an obvious diffraction peak centered at $2\theta = 26.1^{\circ}$, designated to lattice plane (0 0 2) of graphitic carbon (JCPDS 89-8491). Graphitization degree of the deposited carbon is related to its interplanar distance (d_{002}), i.e., the larger interplanar distance, the lower graphitization degree. The graphitization degree was calculated using the Maire and Mering formula: $d = 3.354 + 0.086(1 - g)$, where d is interplanar distance (d_{002}) in angstrom, and g is graphitization percentage [49]. The calculated graphitization degrees of deposited carbon were 40, 44, 46, 58 and 51% for Pd/Al_2O_3, $Pd1Mg/Al_2O_3$, $Pd3Mg/Al_2O_3$, $Pd7Mg/Al_2O_3$ and $Pd10Mg/Al_2O_3$, respectively. Clearly, the highest graphitization degree was for $Pd7Mg/Al_2O_3$ and the lowest for Pd/Al_2O_3. The graphitization degree is most likely related to deposited carbon amount on corresponding spent catalysts (see below TPO results).

The amount and nature of carbon deposition over spent catalysts was investigated by carrying out temperature-programmed oxidation in air (TPO). According to Fig. 11, total amount of deposited carbon as estimated from the peak area of the released CO_2 is 0.0389, 0.0308, 0.0227, 0.0109 and 0.0012 mol/g-catalyst for Pd/Al_2O_3, $Pd1Mg/Al_2O_3$, $Pd3Mg/Al_2O_3$, $Pd10Mg/Al_2O_3$ and $Pd7Mg/Al_2O_3$, respectively. Apparently, one can conclude that promoter Mg significantly suppresses carbon formation on Pd/Al_2O_3, with $Pd7Mg/Al_2O_3$ showing the strongest carbon resistance. Combining with the activity data of catalysts in time on stream (Figs. 5 and 6), the decreasing sequence of the carbon amount on spent catalysts exactly matched the increasing sequence of the conversion values of their reactants. This implies that deposited carbon amount could be a main factor causing catalyst deactivation.

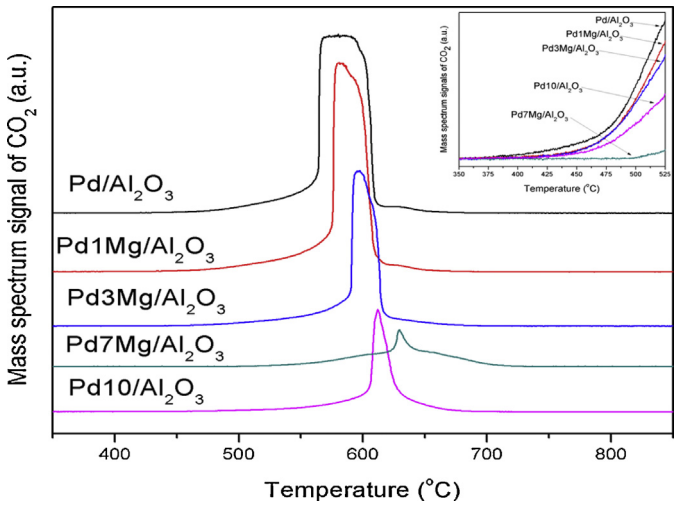

Fig. 11. TPO profiles of spent catalysts.

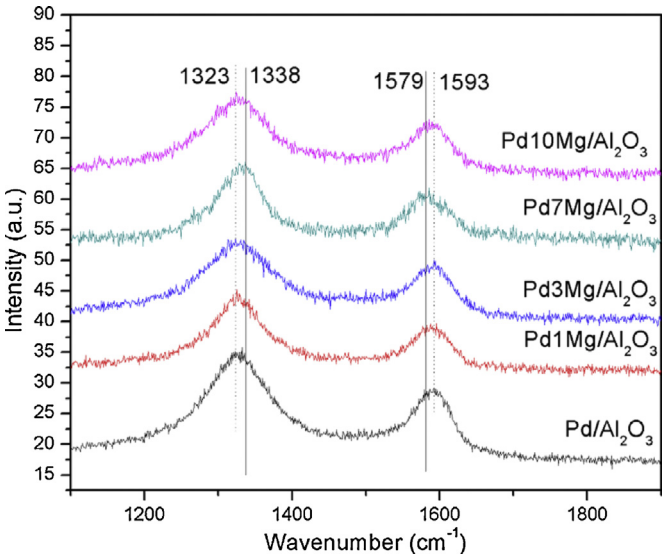

Fig. 12. Raman spectra of spent catalysts.

Each spent catalyst showed a well-defined CO_2 release peak; maximum temperature value at the peak increases in the order: $Pd/Al_2O_3 < Pd1Mg/Al_2O_3 < Pd3Mg/Al_2O_3 < Pd10Mg/Al_2O_3 < Pd7Mg/Al_2O_3$. The order agrees with the increase of graphitization degree for the catalysts. This could be understood due to the fact that carbon deposition with higher crystalline perfection requires higher combustion temperature [50–52]. It is interesting that temperature of carbon combustion on $Pd7Mg/Al_2O_3$ was only above 520 °C. The type of the deposited carbon, therefore, can be mainly in crystalline form [50–52]. However, the CO_2 release over all other catalysts started below 520 °C (see the insert in Fig. 11), and ended at ~680 °C. The CO_2 release below 520 °C is referable to combustion of amorphous carbon; and the estimated carbon amount from the peak area below 520 °C obviously decreased with Mg loading increase. Similar to crystalline carbon deposition, amorphous one can also be suppressed on additive-added catalysts with 7 wt% Mg loading being the most effective. Moreover, each peak contained a steep feature with sudden increasing CO_2 release, suggesting that Pd locates on crystalline carbon and oxidized Pd catalyzes carbon combustion. The finding is similar to previous reports where Ni and Fe can catalytically improve combustion of carbon deposition [52–54].

Raman spectroscopy was used to further explore the structure of carbon species deposited on spent catalysts. As shown in Fig. 12, Raman spectrum of spent catalyst showed two well-defined main bands in the range between 1100 and 1900 cm^{-1}. The band at lower wavenumber is the so-called *D* band associated with the disordered mode of crystalline carbon species, whereas the other at higher wavenumber is the *G* band related to perfect graphite carbon mode [55,56]. It was found that the *D* band was stronger than the *G* band, indicating imperfection of carbon deposition on catalyst. Interestingly, the Raman spectrum of $Pd7Mg/Al_2O_3$ showed a *D* band at 1338 cm^{-1} and a *G* band at 1579 cm^{-1}, respectively, and the two bands had around 15 cm^{-1} of blue shift and 14 cm^{-1} of red shift as compared to those of other catalysts, respectively. To our knowledge, the degree of structural perfection (crystallinity degree) of graphitic carbon species usually could be indicated by either the ratio of I_D/I_G (ratio of intensities of the *D* and *G* bands) or Raman shifts of *D* and *G* bands. The lower the I_D/I_G value, the higher the structural perfection of graphitic carbon [9,57]. *D* band blue shift and *G* band red shift in Raman spectra also imply higher structural perfection of graphitic carbon. Our Raman results fall into the latter category, and are similar to the reported literatures [55,58]. It has been widely reported that the *D* and *G* bands of carbon nanotubes (CNTs) display blue shift and red shift as compared to those of carbon nanofibers (CNFs), respectively [56,58,59]. Therefore, it can be inferred that the carbon deposition on spent $Pd7Mg/Al_2O_3$ presents higher graphitization degree than those on other spent catalysts, agreeing with the XRD and TPO results.

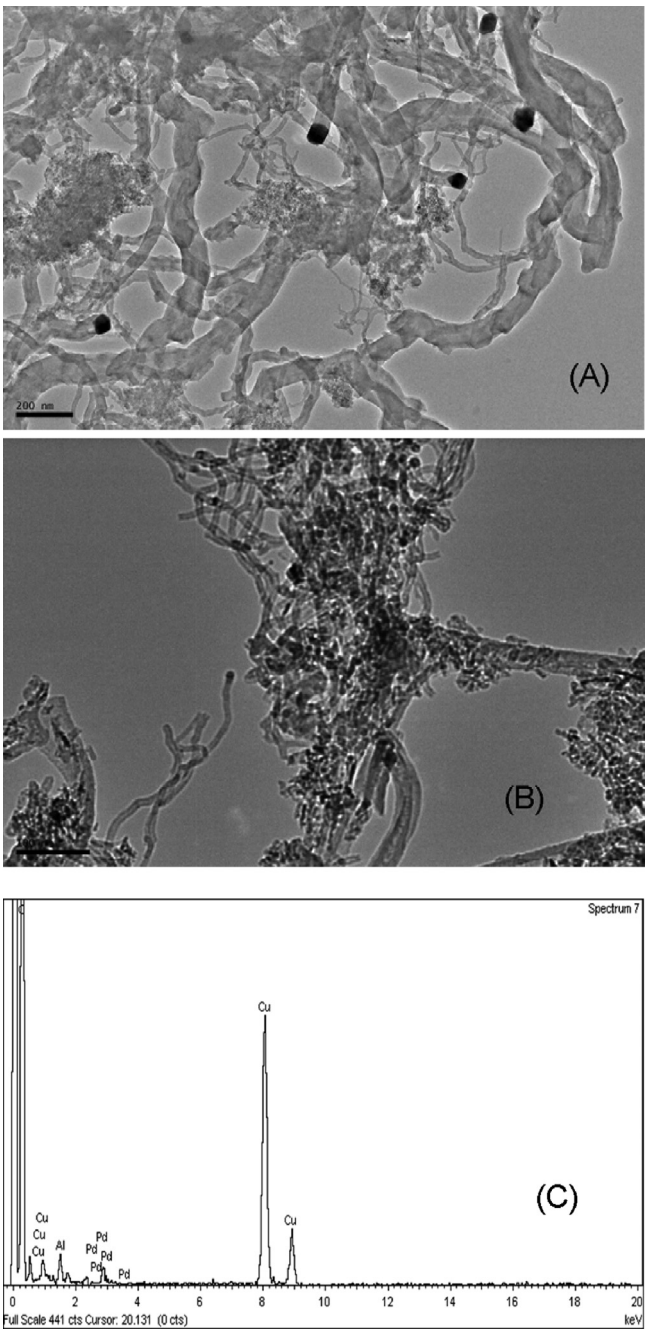

Fig. 13. TEM images and EDX pattern of spent catalysts: (A) Pd/Al_2O_3; (B) $Pd7Mg/Al_2O_3$; (C) EDX pattern.

The carbon deposition and Pd distribution over spent catalysts were also investigated by TEM. Obtained results support the aforementioned observations in the XRD, TPO and Raman studies. As presented in Fig. 13, carbon deposition over spent MgO-free Pd/Al_2O_3 was a mixture of CNTs, CNFs and amorphous carbon, whereas only CNTs were observed for spent $Pd7Mg/Al_2O_3$. The filaments were tangled together to form very sinuous carbon species on spent catalysts. The CNTs were in the form of multi-

walled carbon nanotubes (MWCNTs). Addition of promoter Mg to Pd/Al_2O_3 considerably suppressed production of filament carbon and improved the uniformity of deposited carbon. Compared to the uneven distribution of filaments with some in 50–80 nm of tube diameter for Pd/Al_2O_3, uniform distribution of CNTs with $11 \sim 12$ nm was found for $Pd7Mg/Al_2O_3$. It can be also seen that metallic Pd nanoparticles, confirmed by EDX spectra (Fig. 13), located at the tips of the carbon filament. The Pd nanoparticle and its grown carbon filament had same diameter size. The result is similar to those reported in the literatures [60,61], where the diameters of the carbon filaments are strongly dependent on the size of metal nanoparticles serving as catalyst. Moreover, it should be mentioned that no filament carbon was observed on Pd particles whose size were smaller than ~10 nm, implying small metal particles could totally suppress carbon deposition in the methane reforming process.

3.5. Effects of additive MgO on catalytic performance of Pd catalysts

Based on the above evaluation and characterization results of the catalysts, it is clear that the activity and stability of Mg-modified Pd/Al_2O_3 catalysts in the methane reforming of carbon dioxide depended on the Mg loading, and significant improvement was observed for $Pd7Mg/Al_2O_3$. Addition of MgO notably influences surface properties of the catalyst, including thermal stability of Pd oxides, metallic surface dispersion and particle size, metal sintering and carbon resistances. These surface properties could essentially account for the catalytic performance of the catalysts [8,14–22,62,63]. The XRD results identified that MgO mainly exist as amorphous type on catalysts with Mg loading no more than 7 wt%. The amorphous oxide remarkably modifies surface characteristics of the catalyst. It increased thermal decomposition temperature of Pd oxides, as indicated in the O_2-TPD results. The highest decomposition temperature of Pd oxides on $Pd7Mg/Al_2O_3$ confirmed a kind of interaction between metal and support occurs. The CO-chemisorption and XRD results showed the highest metal dispersion and the smallest crystallite size on $Pd7Mg/Al_2O_3$. Obviously, high Pd dispersion and small particle size offer more accessible active sites, where methane dissociation occurs and is regarded as a structure–sensitive reaction and a rate-controlling step in methane reforming with carbon dioxide [3,13,14]. CH_4 activation on Pd surface, therefore, would be improved. In addition, high Pd dispersion and small particle size also provide more interfacial area between Pd and MgO, where reactant, CO_2, help efficiently oxidize carbon produced on metal by methane decomposition. In this way, methane reforming with carbon dioxide over MgO promoted Pd catalysts could be maintained at high efficiency. Similar activation effect has been extensively reported for Ni and Pt catalysts in CO_2 reforming of methane, where CO_2 is activated in the proximity of metal particles and then reacts with methane activated on the metals [64–68]. Therefore, the enhanced catalytic activity of Mg-added catalysts is mainly associated with enhanced Pd dispersion as well as increased concentration of interfacial area of Pd–MgO.

It is generally believed that carbon deposit and metal sintering, both of which would decrease accessible active metal sites via covering effect and agglomeration effect, are two main reasons causing catalyst deactivation during the methane reforming process [3,4,8,20,22,67–69]. The amount and kind of carbon deposition are closely associated with the metal particle size. The XRD and TEM results show that metal particles on Pd/Al_2O_3 can be easily sintered to large Pd clusters, which not only decrease active metallic surface area but also are prone to fast carbon deposition. The largest amount of carbon deposition in the forms of amorphous carbon, long and large CNFs and CNTs were confirmed on Pd/Al_2O_3 by TPO, Raman and TEM techniques. They would cover catalyst surface and block accessible Pd active sites, resulting in its fast deactivation. The amorphous carbon on the Pd catalyst could encapsulate exposed active metal particles, resulting in its significant deactivation, similar to the previously reported Ni catalysts [68–72]. In contrast, promoter Mg on Pd catalysts remarkably affects the two main deactivation factors. Introduction of MgO to Pd/Al_2O_3 effectively strengthens interaction between Pd and support, thus improves surface Pd dispersion and decreases metal particle size. It is believed that the small metal particle has strengthened the capability of sintering resistance and is able to suppress carbon deposition in the reforming process [22,27,62,73]. Average crystallite size of 11.7 nm over $Pd7Mg/Al_2O_3$ was identified by XRD, which is close to the reported threshold values of metal particles suggested to completely suppress carbon deposition in the methane reforming with carbon dioxide [20,22]. As a result, the highest catalytic stability of $Pd7Mg/Al_2O_3$ was observed, which coincides with the smallest size of Pd particles, the lowest amount of deposited carbon and the best crystalline perfection of carbon. Moreover, relatively small metal particles are prone to form small and short CNTs with higher crystalline perfection than CNFs and amorphous carbon (see XRD, Raman and TEM results). Pd particles are located at the end of the CNTs and the active sites are still exposed to reactants. The carbon form with crystalline perfection could be removed easily and is suggested to improve catalytic stability in CO_2 reforming of methane [74]. Therefore, an optimal Mg loading is required to stabilize small Pd particles to obtain the best catalytic performance.

On the other hand, excessive Mg loading results in transformation of partial amorphous MgO into crystalline ones, as confirmed by XRD. In contrast to the dispersion effect of amorphous MgO on surface Pd improving sintering resistance of metal particle, the crystalline MgO covers a portion of the exposed Pd surface due to the decoration effect and promote its sintering in time on stream. Moreover, excessive Mg loading caused significant drop in the specific surface area, pore volume and size of catalyst due to strong interaction between basic MgO and acid support. The deterioration of textural characteristics on catalyst with the highest Mg loading could also contribute to Pd particle sintering. Consequently, exposed active Pd sites decrease and carbon deposition increases. This could account for the lower activity and worse stability of $Pd10Mg/Al_2O_3$ than $Pd7Mg/Al_2O_3$.

In summary, the highest activity and best stability of $Pd7Mg/Al_2O_3$ over others could be attributed to the highest Pd dispersion, the highest interfacial area between Pd and MgO as well as the strongest resistances to both metal sintering and carbon deposition.

4. Conclusion

Depending on the additive loading, Mg-modified Pd/Al_2O_3 demonstrates remarkably enhanced initial activity, long-term stability as well as yields of hydrogen and carbon monoxide in carbon dioxide reforming of methane. When Mg loading is below 7 wt%, amorphous MgO on the catalysts improves surface Pd dispersion, decreases metal particle size and increases interfacial area of Pd–MgO, leading to increased active sites, strong metal sintering resistance, decreased carbon deposition and enhanced graphitization degree. The promotion effect increases with increased Mg content. The best catalytic performance, therefore, is observed on $Pd7Mg/Al_2O_3$. On the other hand, with Mg content at 10 wt%, a part of amorphous MgO on catalysts is turned into crystalline one, which not only decreases exposed Pd active sites through its decoration effect on metal but also causes significant decline in support characteristics, accelerating surface metal sintering and carbon

deposition. Consequently, worse catalytic performance is observed for Pd10Mg/Al_2O_3 as compared with Pd7Mg/Al_2O_3.

Acknowledgments

Support from the US Department of Energy (DE-FC26-05NT42457) and the National Science Foundation (CHE-0632071) are greatly acknowledged.

References

[1] J.D. Figueroa, T. Fout, S. Plasynski, H. McIlvried, R.D. Srivastava, Int. J. Greenhouse Gas Control 2 (2008) 9–20.
[2] http://www2.epa.gov/carbon-pollution-standards/learn-about-carbon-pollution-power-plants
[3] M.C.J. Bradford, M.A. Vannice, Catal. Rev. Sci. Eng. 41 (1999) 1–42.
[4] Y.H. Hu, E. Ruckenstein, Adv. Catal. 48 (2004) 297–345.
[5] J.H. Horlock, Combined Power Plants, Pergamon Press, Oxford, 1992.
[6] M.M.V.M. Souza, D.A.G. Aranda, M. Schmal, J. Catal. 204 (2001) 498–511.
[7] D. Lee, P. Hacarlioglu, S.T. Oyama, Top. Catal. 29 (2004) 45–57.
[8] J.M. García-Vargas, J.L. Valverde, J. Díez, P. Sánchez, F. Dorado, Appl. Catal. B 164 (2015) 316–323.
[9] M.H. Amin, K. Mantri, J. Newnham, J. Tardio, S.K. Bhargava, Appl. Catal. B 119–120 (2012) 217–226.
[10] R. Pereñiguez, V.M. Gonzalez-delaCruz, A. Caballero, J.P. Holgado, Appl. Catal. B 123–124 (2012) 324–332.
[11] R. Bouarab, O. Akdim, A. Auroux, O. Cherifi, C. Mirodatos, Appl. Catal. A 264 (2004) 161–168.
[12] D. San-Jose-Alonso, J. Juan-Juan, M.J. Illan-Gomez, M.C. Roman-Martinez, App. Catal. A 371 (2009) 54–59.
[13] E. Ruckenstein, H.Y. Wang, J. Catal. 205 (2002) 289–293.
[14] A. Yamaguchi, E. Iglesia, J. Catal. 274 (2010) 52–63.
[15] H. Masai, A. Kado, A. Miyake, S. Nishiyama, S. Tsuruya, Stud. Surf. Sci. Catal. 36 (1988) 67–71.
[16] F. Solymosi, A. Erdohelyi, J. Cserenyi, Catal. Lett. 16 (1992) 399–405.
[17] A. Erdohelyi, J. Cserenyi, E. Papp, F. Solymosi, Appl. Catal. A 108 (1994) 205–219.
[18] P.G. Schulz, M.G. Gonzalez, C.E. Quincoces, C.E. Gigola, Ind. Eng. Chem. Res. 44 (2005) 9020–9029.
[19] B. Steinhauer, M.R. Kasireddy, J. Radnik, A. Martin, Appl. Catal. A 366 (2009) 333–341.
[20] C. Shi, P. Zhang, Appl. Catal. B 115–116 (2012) 190–200.
[21] K. Nagaoka, K. Aika, Bull. Chem. Soc. Jpn. 74 (2001) 1841–1846.
[22] S. Damyanova, B. Pawelec, K. Arishtirova, J.L.G. Fierro, C. Sener, T. Dogu, Appl. Catal. B 92 (2009) 250–261.
[23] M. Masai, H. Kado, A. Miyake, S. Nishiyama, S. Tsuruya, Stud. Surf. Sci. Catal. 36 (1988) 67–71.
[24] I.H. Son, S.J. Lee, H.S. Roh, Int. J. Hydrogen Energy 39 (2014) 3762–3770.
[25] L. Xu, H. Song, L. Chou, Appl. Catal. B 108–109 (2011) 177–190.
[26] J. Zhu, X. Peng, L. Yao, J. Shen, D. Tong, C. Hu, Int. J. Hydrogen Energy 36 (2011) 7094–7104.
[27] H. Jeong, K.I. Kim, D. Kim, I.K. Song, J. Mol. Catal. A 246 (2006) 43–48.
[28] L.F. Yang, C. Shi, X. He, J.X. Cai, Appl. Catal. B 38 (2002) 117–125.
[29] Y. He, L. Liang, Y. Liu, J. Feng, C. Ma, D. Li, J. Catal. 309 (2014) 166–173.
[30] Y. Diao, R. Yan, S. Zhang, P. Yang, Z. Li, L. Wang, H. Dong, J. Mol. Catal. A 303 (2009) 35–42.
[31] K.S.W. Sing, D.H. Everett, R.A.W. Haul, L. Moscou, R.A. Pierotti, J. Rouquerol, T. Siemieniewska, International union of pure and applied chemistry, IUPAC, Pure Appl. Chem. 57 (1985) 603–619.
[32] M.M.V.M. Souza, D.A.G. Aranda, M. Schmal, J. Catal. 204 (2001) 498–511.
[33] E.B. Fox, S. Velua, M.H. Engelhard, Y.H. Chin, J.T. Miller, J. Kropf, C. Song, J. Catal. 260 (2008) 358–370.
[34] L. Bollmann, J.L. Ratts, A.M. Joshi, W.D. Williams, J. Pazmino, Y.V. Joshi, J.T. Miller, A.J. Kropf, W.N. Delgass, F.H. Ribeiro, J. Catal. 257 (2008) 43–54.
[35] R.S. Monteiro, L.C. Dieguez, M. Schmal, Catal. Today 65 (2001) 77–89.
[36] J.C.S. Araujo, D. Zanchet, R. Rinaldi, U. Schuchardt, C.E. Hori, J.L.G. Fierro, J.M.C. Bueno, Appl. Catal. B 84 (2008) 552–562.
[37] G. Wang, M. Meng, Y. Zha, T. Ding, Fuel 89 (2010) 2244–2251.
[38] F. Klingstedt, A.K. Neyestanaki, R. Byggningsbacka, L.E. Lindfors, M. Lundén, M. Petersson, P. Tengström, T. Ollonqvist, J. Väyrynen, Appl. Catal. A 209 (2001) 301–316.
[39] C. Shi, L. Yang, Z. Wang, J. Cai, G. Li, X. Wang, Appl. Catal. A 243 (2003) 379–388.
[40] W.E. Bell, R.E. Inyard, M. Tagami, J. Phys. Chem. 70 (1966) 3735–3736.
[41] J.G. McCarty, Catal. Today 26 (1995) 283–293.
[42] H. Lieske, J. Volter, J. Phys. Chem. 89 (1985) 1841–1842.
[43] A.H. Fakeeha, M.A. Naeem, W.U. Khan, A.S. Al-Fatesh, J. Ind. Eng. Chem. 20 (2014) 549–557.
[44] J. Juan-Juan, M.C. Roman-Martinez, M.J. Illan-Gomez, Appl. Catal. A 355 (2009) 27–32.
[45] R. Zanganeh, M. Rezaei, A. Zamaniyan, Int. J. Hydrogen Energy 38 (2013) 3012–3018.
[46] J.D.A. Bellido, J.E. De Souza, J.M. Peko, E.M. Assaf, Appl. Catal. A 358 (2009) 215–223.
[47] J.H. Edwards, A.M. Maitra, Fuel Process. Technol. 42 (1995) 269–289.
[48] J. Zhang, H. Wang, A.K. Dalai, J. Catal. 249 (2007) 300–310.
[49] J. Maire, J. Mering. In Proceeding 4th Biennial American Carbon Conference, 1960, p. 345.
[50] Z. Yu, D. Chen, M. Rønning, B. Tøtdal, T. Vralstad, E. Ochoa-Fernandez, A. Holmen, Appl. Catal. A 338 (2008) 147–158.
[51] M.R. Cuervo, E. Asedegbega-Nieto, E. Díaz, S. Ordóñez, A. Vega, A.B. Dongil, I. Rodríguez-Ramos, Carbon 46 (2008) 2096–2106.
[52] J.W. Long, M. Laskoski, T.M. Keller, K.A. Pettigrew, T.N. Zimmerman, S.B. Qadri, G.W. Peterson, Carbon 48 (2010) 501–508.
[53] B.J. Landi, C.D. Cress, C.M. Evans, R.P. Raffaelle, Chem. Mater. 17 (2005) 6819–6834.
[54] V.M. Irurzun, M.P. Ruiz, D.E. Resasco, Carbon 48 (2010) 2873–2881.
[55] M. García-Diéguez, I.S. Pieta, M.C. Herrera, M.A. Larrubia, L.J. Alemany, J. Catal. 270 (2010) 136–145.
[56] H. Zhang, G. Lin, Z. Zhou, X. Dong, T. Chen, Carbon 40 (2002) 2429–2436.
[57] A. Serrano-Lotina, L. Daza, Appl. Catal. A 474 (2014) 107–113.
[58] Y. Liu, C. Pan, J. Wang, J. Mater. Sci. 39 (2004) 1091–1094.
[59] P.C. Eklund, J.M. Holden, R.A. Jishi, Carbon 33 (1995) 959–972.
[60] T.V. Choudhary, E. Aksoylu, D.W. Goodman, Catal. Rev. Sci. Eng. 45 (2003) 151–203.
[61] D. Chen, K.O. Christensen, E. Ochoa-Fernández, Z. Yu, B. Tøtdal, N. Latorre, A. Monzón, A. Holmen, J. Catal. 229 (2005) 82–96.
[62] S. Sokolov, E.V. Kondratenko, M.M. Pohl, A. Barkschat, U. Rodemerck, Appl. Catal. B 113–114 (2012) 19–30.
[63] M.O. Abba, V.M. Gonzalez-DelaCruz, G. Colon, S. Sebti, A. Caballero, Appl. Catal. B 150–151 (2014) 459–465.
[64] J.H. Bitter, K. Seshan, J.A. Lercher, J. Catal. 176 (1998) 93–101.
[65] J.H. Bitter, K. Seshan, J.A. Lercher, J. Catal. 171 (1997) 279–286.
[66] S.M. Stagg-Williams, F.B. Noronha, G. Fendley, D.E. Resasco, J. Catal. 194 (2000) 240–249.
[67] B. Bachiller-Baeza, C. Mateos-Pedrero, M.A. Soria, A. Guerrero-Ruiz, U. Rodemerck, I. Rodríguez-Ramos, Appl. Catal. B 129 (2013) 450–459.
[68] R. Yang, C. Xing, C. Lv, L. Shi, N. Tsubaki, Appl. Catal. A 385 (2010) 92–100.
[69] L. Ji, S. Tang, H.C. Zeng, J. Lin, K.L. Tan, Appl. Catal. A 207 (2001) 247–255.
[70] A. Horváth, G. Stefler, O. Geszti, A. Kienneman, A. Pietraszek, L. Guczi, Catal. Today 169 (1) (2011) 102–111.
[71] X. Zhu, P. Huo, Y. Zhang, D. Cheng, C. Liu, Appl. Catal. B 81 (2008) 132–140.
[72] M. Matsukata, T. Matsushita, K. Ueyama, Energy Fuel 9 (1995) 822–828.
[73] T. Osaki, T. Mori, J. Catal. 204 (2001) 89–97.
[74] Y. Qu, A.M. Sutherland, T. Guo, Energy Fuel 22 (2008) 2183–2187.